Electronic Supplementary Information (ESI)†

Montmorillonite Nanoreactors for Synergistic Confinement Synthesis and Ion-Conduction in Stable Sulfurized Polyacrylonitrile Cathodes

Yihui Li,[a,#] Chenyu Yan,[a,#] Xiongbo Dong,[a] Kaiyang Zheng,[a] Zehui Yang,[a] Sanle Shan,[a] Aidong Tang [a,b,c*], Xiangxiong Chen, [b,c*] Huaming Yang [a]

[a] Engineering Research Center of Nano-Geomaterials of Ministry of Education, Laboratory of Advanced Mineral Materials, and Faculty of Materials Science and Chemistry, China University of Geosciences, Wuhan 430074, China;

[b] College of Chemistry and Chemical Engineering, Central South University, Changsha 410083, China;

[c] Hunan Key Laboratory of Chemical Power Source, Central South University, Changsha 410083, China;

*Corresponding authors:

E-mail address: adtang@csu.edu.cn and tangaidong@cug.edu.cn (A. T.);

30663804@qq.com (X. C.)

Experimental Section in Detail

1. Detailed Synthesis Procedures

Purification of AN: 10 mL of AN was mixed with 1 mL of 1 M NaOH solution. After stirring, the mixture was allowed to settle, and the lower NaOH layer was discarded to obtain inhibitor-free AN.

Dispersion of MMT: 0.5 g of MMT was dissolved in 100 mL of deionized water. The dispersion was subjected to high-speed magnetic stirring for 1 h followed by ultrasonication for 1 h. This cycle was repeated 6 times to ensure complete exfoliation.

In-situ polymerization to synthesize PAN/MMT: First, remove the polymerization inhibitor from acrylonitrile (AN). Add AN to 1 mL of 1 mol·L-1 NaOH solution and stir. Pour it into a separating funnel. Let the solution stand and separate. Discard the lower layer of NaOH. This will give you the AN with the polymerization inhibitor removed. Dissolve 0.5 g of montmorillonite (MMT) in 100 mL of deionized water and stir at high speed with a magnetic stirrer for 1 hour. Then, ultrasonicate for 1 hour. Repeat this process several times to ensure that MMT is fully dispersed. Add the AN solution with the polymerization inhibitor removed to the MMT dispersion solution and ultrasonicate for 1 hour. Then, add azobisisobutyronitrile (AIBN) as the polymerization initiator. Stir vigorously in a 70 ℃ water bath. After the reaction, centrifuge and dry at 80 ℃ under vacuum to obtain the solid, named PAN/MMT.

Sulfurization synthesis of SPAN/MMT: Take 0.2 g of PAN/MMT solid and 1.6 g of sulfur powder, mix and grind for 30 minutes to form a powder. Put it in a porcelain boat, and heat it in a tubular furnace under nitrogen atmosphere at a heating rate of 2 ℃/min to 300 ℃, and keep it at this temperature for 300 minutes. After the reaction, collect the obtained solid, grind it into powder, and heat it in the

tubular furnace under nitrogen atmosphere at a heating rate of 2 ℃/min to 300 ℃, and keep it at this temperature for 180 minutes. After the reaction, the obtained powder is SPAN/MMT. The synthesis of pure SPAN is the same as the above method, except that MMT is not added.

Battery Fabrication: The cathode slurry was prepared by mixing the active material (SPAN/MMT), conductive carbon (Super P), and poly(vinylidene fluoride) (PVDF) binder in a mass ratio of 7:2:1 using N-methyl-2-pyrrolidone (NMP) as the solvent. The slurry was coated onto carbon-coated aluminum foil. The mass loading of the active material was approximately 1.5-2.0 mg cm^{-2}. CR2032 coin cells were assembled using a lithium metal foil as the counter electrode, a Celgard 2500 membrane as the separator, and 1 M LiTFSI in a mixture of 1,3-dioxolane (DOL) and 1,2-dimethoxyethane (DME) (1:1 by volume) with 1 wt% $LiNO_3$ as the electrolyte. All assembly procedures were conducted in an Ar-filled glove box (H_2O/O_2 < 0.1 ppm).

2. Detailed Characterization Methods

XRD was performed with a scanning rate of 5° min^{-1} in the 2θ range of 5–80°.

XPS spectra were acquired using an Al Kα X-ray source and calibrated by referencing the C 1s peak to 284.8 eV.

For **SEM** and **TEM** observations, the samples were dispersed in ethanol and dropped onto a silicon wafer or a copper grid, respectively.

Raman spectra were recorded with a 633 nm laser excitation.

For **BET** measurements, the samples were degassed under vacuum at 120 °C for 12 h prior to analysis.

3. Detailed Electrochemical Measurements

Galvanostatic charge/discharge tests were carried out on a LAND battery test system within a voltage window of 1-3 V (vs. Li^+/Li).

CV and **EIS** measurements were conducted on a CHI760 electrochemical workstation. CV tests were performed at a scan rate of 0.1 mV s^{-1}. EIS spectra were recorded over a frequency range from 100 kHz to 0.01 Hz with an amplitude of 5 mV.

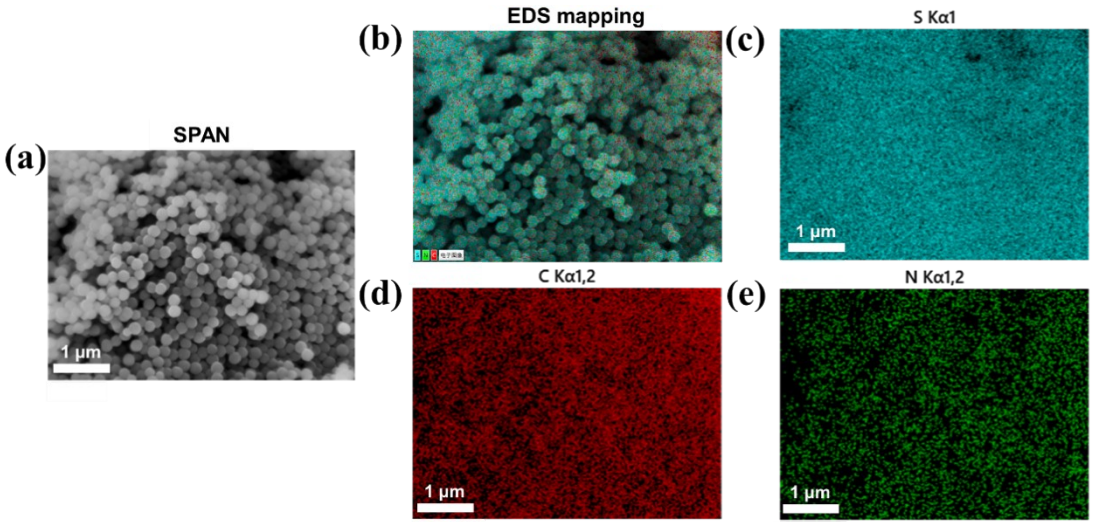

Figure S1. (a) SEM image of pure SPAN. (b) Elemental mapping images of SPAN for S, C, and N (c-e).

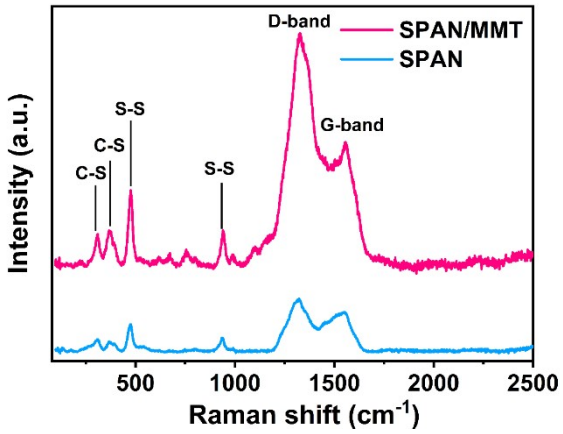

Figure S2. Raman spectra of SPAN and SPAN/MMT.

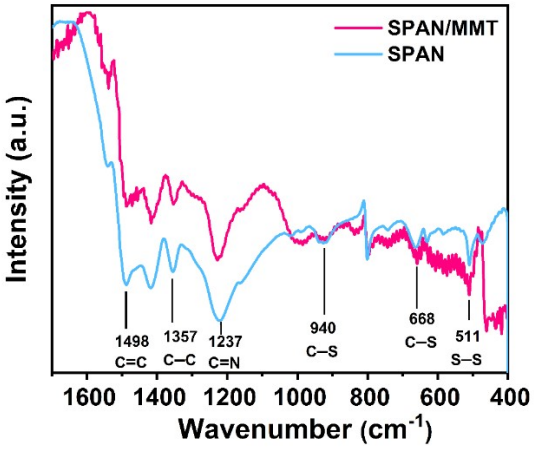

Figure S3. FTIR spectra of SPAN and SPAN/MMT.

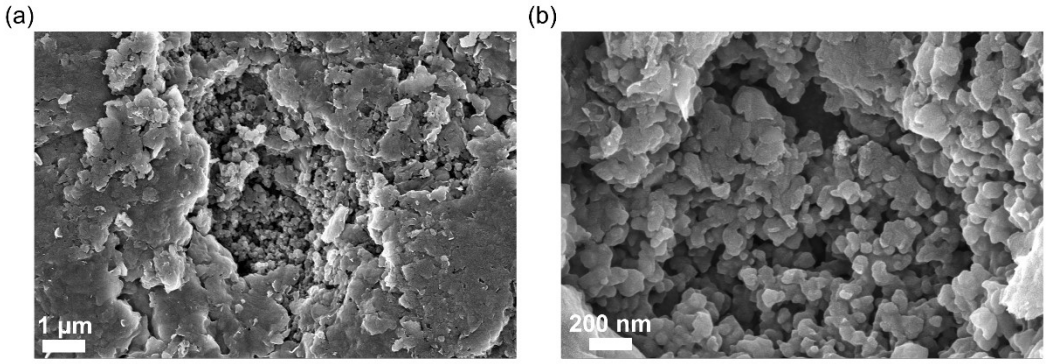

Figure S4. SEM images of SPAN/MMT at different magnifications, showing the SPAN aggregate within an MMT cavity.

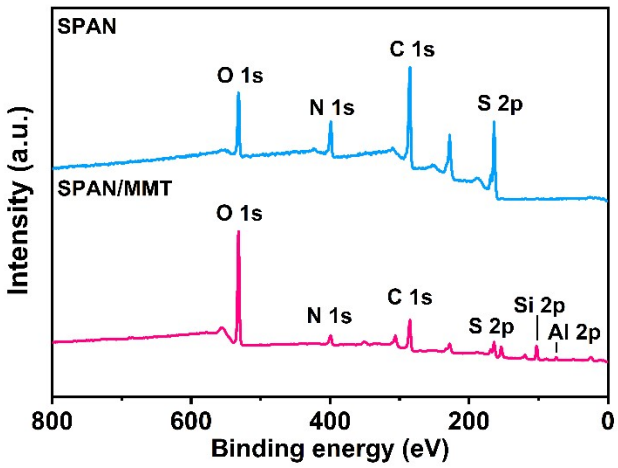

Figure S5. XPS survey spectra of SPAN and SPAN/MMT.

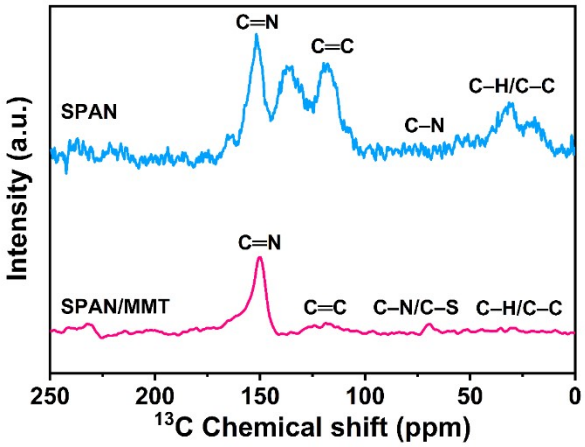

Figure S6. ^{13}C CP-MAS ssNMR spectra of SPAN and SPAN/MMT.

Notes S1. Detailed Discussion on SEM, FTIR, Raman, and XPS Results

This section provides a detailed discussion of the characterization results presented in Figures S1-S5, offering further support for the conclusions drawn in the main text.

SEM Analysis (Fig. S1, S4):

Scanning Electron Microscopy (SEM) results reveal distinct morphological differences between the materials. Pure SPAN (Fig. S1) exhibits a regular spherical particle morphology. In contrast, the SPAN/MMT composite (main text Fig. 1c, ESI Fig. S4) retains the characteristic layered structure of MMT. More significantly, high-magnification SEM images of SPAN/MMT (Fig. S4) show SPAN aggregates residing within the interlayer gaps of MMT, providing direct morphological evidence for the in-situ polymerization and confined sulfurization. Furthermore, cross-sectional SEM images of the SPAN/MMT electrode (Fig. S10) indicate a more intimate contact with the current collector, which is beneficial for reducing interfacial resistance and enhancing structural integrity.

FTIR Analysis (Fig. S3):

Fourier-Transform Infrared (FTIR) spectroscopy confirms the successful formation of characteristic functional groups in SPAN. The characteristic peaks at 511 cm^{-1} (S-S bond), 668 cm^{-1}, and 940 cm^{-1} (C-S bonds) in both SPAN and SPAN/MMT verify the successful sulfurization process. Concurrently, the absorption peaks at 1237 cm^{-1} (C=N bond), 1498 cm^{-1} (C=C bond), and 801 cm^{-1} (breathing vibration of the six-membered ring) collectively demonstrate the formation of a conjugated heterocyclic

structure derived from cyclized PAN. The high similarity between the FTIR spectra of SPAN/MMT and pure SPAN indicates that the introduction of MMT does not alter the fundamental chemical structure of SPAN, but primarily provides a nanoconfined physical environment.

Raman Analysis (Fig. S2, Table S1):

Raman spectroscopy offers key insights into the graphitization degree of the materials. The significantly higher ID/IG ratio of SPAN/MMT (1.88) compared to pure SPAN (1.33) indicates a lower degree of graphitization, implying a more disordered carbon skeleton with a greater number of defects. This finding is consistent with the increase in the C-N/C=N ratio observed in the XPS N 1s spectra (main text Fig. 2b). This higher defect density likely originates from the restricted, ordered stacking of SPAN molecular chains within the confined interlayer space of MMT. It is noteworthy that this disordered structure may help accommodate volume strain during charge/discharge cycles, thereby contributing to the exceptional structural stability.

In summary,a combination of characterization techniques conclusively verifies the successful preparation of the SPAN/MMT composite: MMT acts as a nano-scaffold providing confinement space, within which SPAN is successfully formed while retaining its basic chemical structure. Simultaneously, this unique synthesis pathway results in a higher defect density and distinct morphology, which synergistically contribute to the outstanding electrochemical performance.

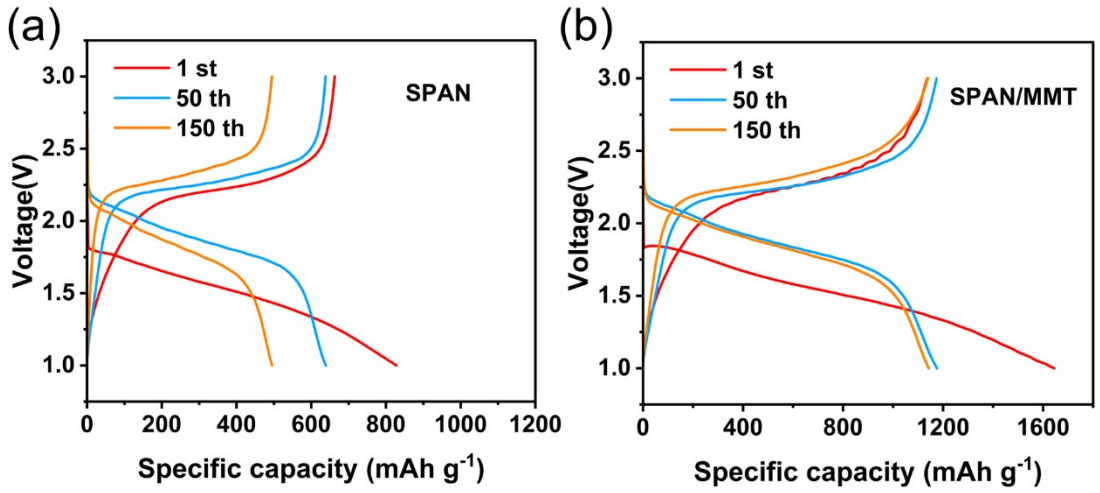

Figure S7. Galvanostatic charge-discharge voltage profiles of (a)SPAN and (b)SPAN/MMT at various cycles.

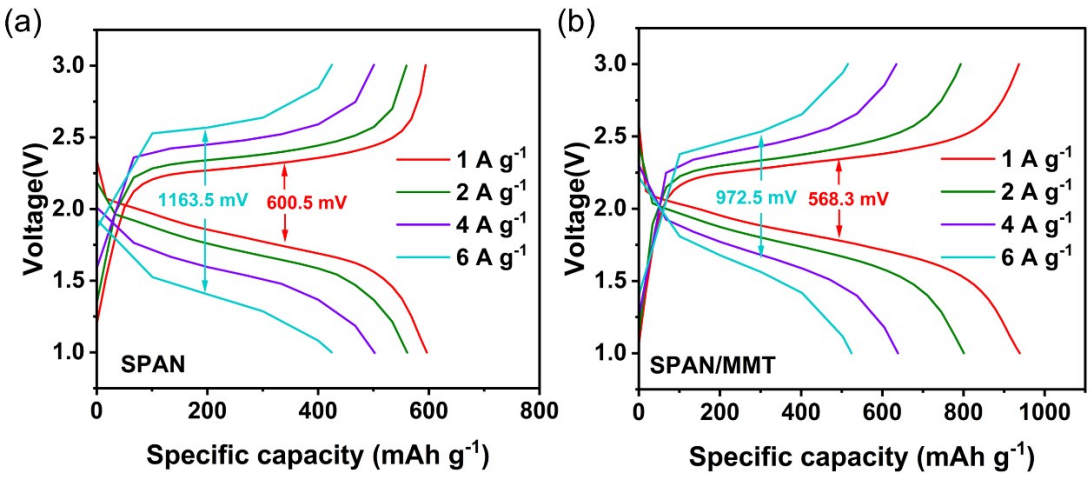

Figure S8. Galvanostatic charge-discharge voltage profiles of (a) SPAN and (b) SPAN/MMT at various current densities

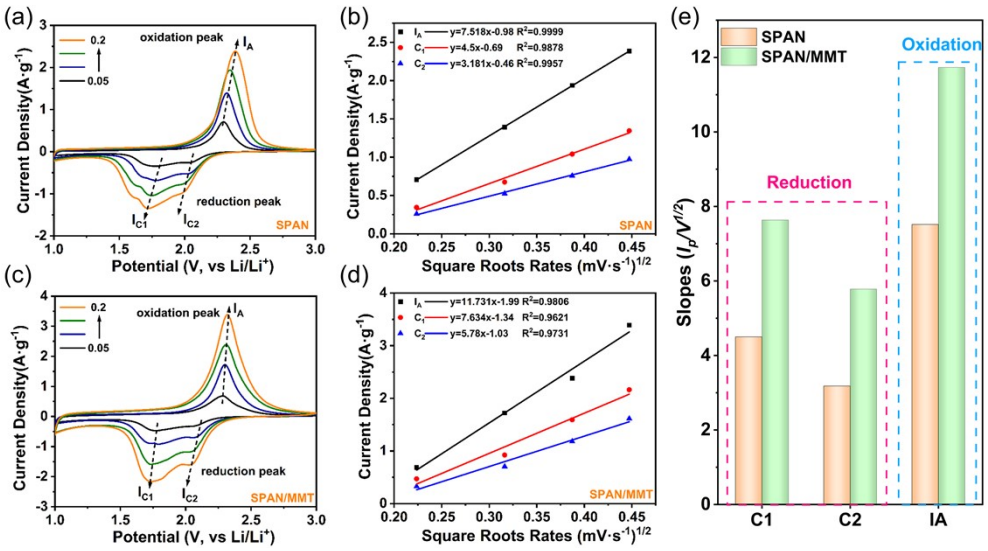

Figure S9. CV curves at different scan rates for (a) SPAN and (c) SPAN/MMT. Linear fits of the peak current density vs. square root of scan rate for (b) SPAN and (d) SPAN/MMT. (e) Bar chart of the corresponding current density and the slope of the square root of the rate curve.

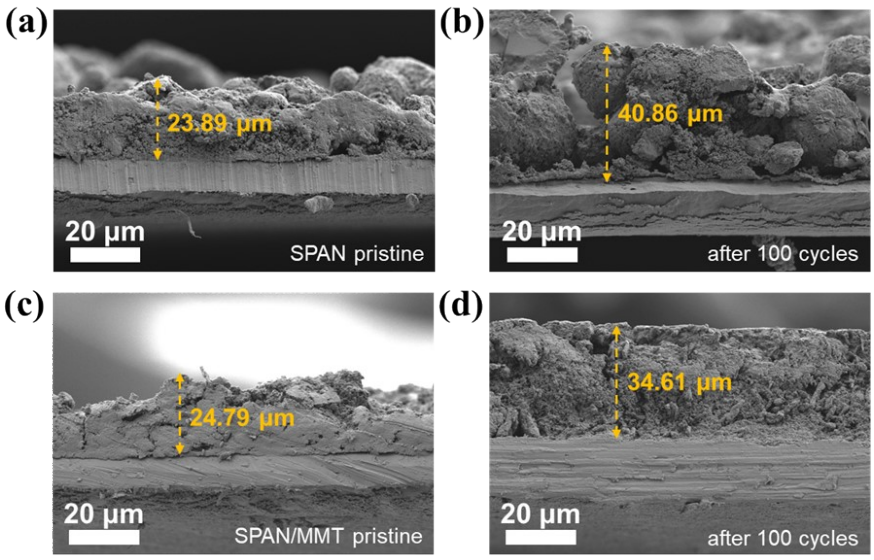

Figure S10. Cross-sectional SEM images of (a, b) pristine and cycled SPAN cathodes, and (c, d) pristine and cycled SPAN/MMT cathodes.

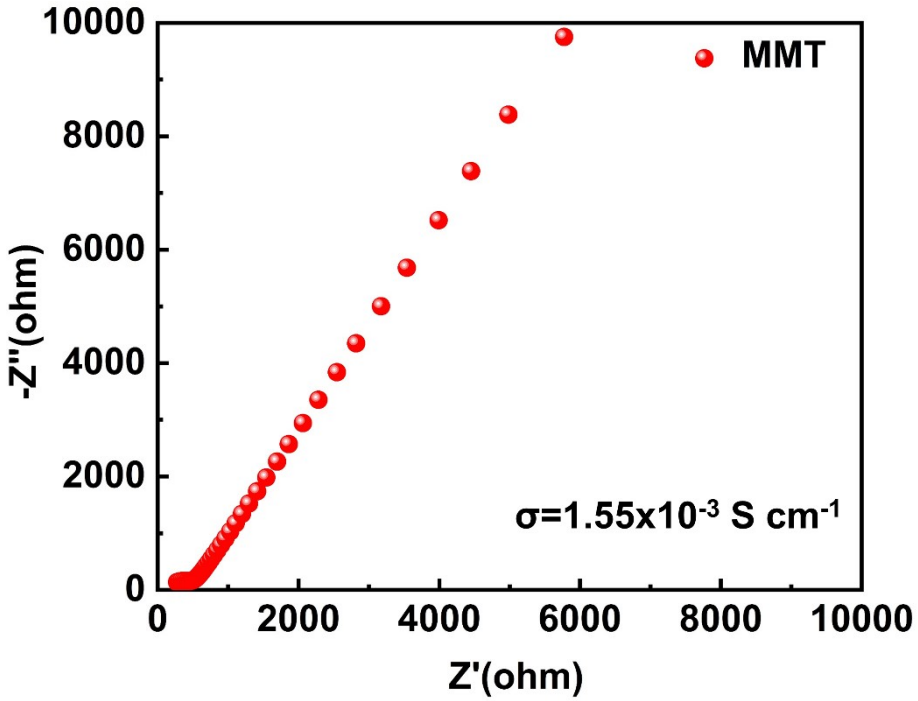

Figure S11. Nyquist plot and ionic conductivity of a compacted MMT powder measured at room temperature

Notes S2. Detailed discussion on the electrochemical performance.

This section provides a detailed discussion and supplementary data from the electrochemical performance tests to further support the conclusions drawn in the main text.

Rate Performance in Detail

As shown in Fig. 3c of the main text, the SPAN/MMT cathode exhibits outstanding rate capability. The specific discharge capacities at various current densities are as follows: 1250 mAh g^{-1} at 0.2 A g^{-1}, 1122 mAh g^{-1} at 0.4 A g^{-1}, 996 mAh g^{-1} at 0.8 A g^{-1}, 938 mAh g^{-1} at 1 A g^{-1}, 801 mAh g^{-1} at 2 A g^{-1}, 638 mAh g^{-1} at 4 A g^{-1}, and 524 mAh g^{-1} at the extremely high rate of 6 A g^{-1}. When the current density was returned to 0.4 A g^{-1} and subsequently to 0.2 A g^{-1}, the capacity recovered to 1055 mAh g^{-1} and 1185 mAh g^{-1}, respectively, regaining 95% of the initial capacity. This exceptional recoverability indicates that the electrode structure remains highly intact and exhibits superb reversibility even after high-rate cycling. In contrast, the pure SPAN cathode delivered significantly lower capacities at all identical current densities, underscoring the critical role of MMT in enhancing the reaction kinetics.

The galvanostatic charge–discharge voltage profiles at various current densities (Fig. S8) offer further insight into the polarization behavior and kinetic limitations of the electrodes. As the current density increases from 1 to 6 A g^{-1}, both cathodes exhibit a gradual decrease in discharge plateau voltage and an increase in voltage hysteresis, indicating enhanced polarization under high-rate conditions. For the pure SPAN material (Fig. S8a), the polarization voltage reached 1163.5 mV at a current density of

6 A g^{-1}, accompanied by a significant drop in the discharge plateau. This indicates severe kinetic limitations and sluggish lithium-ion transport within the electrode. In contrast, the SPAN/MMT composite (Fig. S8b) exhibited a markedly lower polarization voltage of 972.5 mV at 6 A g^{-1} and maintained a more distinct discharge plateau even under such a high current density. The improved electrochemical performance of SPAN/MMT intuitively demonstrates that the MMT nanoreactor effectively mitigates electrode polarization and underscores the role of MMT in enhancing ion transport and reaction reversibility at extremely high rates.

Failure Analysis of Pure SPAN

The long-term cycling performance of the pure SPAN cathode at 1 A g^{-1} (Fig. 3b) further reveals its structural instability. Its initial reversible discharge capacity was 710 mAh g^{-1}. After 652 cycles, the capacity decayed to 184.6 mAh g^{-1}, followed by rapid battery failure. This rapid capacity fade is directly linked to the deterioration of the electrode structure. As observed in the post-cycling SEM images (Fig. S10 a,b), the SPAN electrode suffered severe expansion (71%) and pulverization, leading to the detachment of active material from the conductive network. This stands in stark contrast to the stable 5000-cycle performance of SPAN/MMT at 3 A g^{-1}, conclusively demonstrating the decisive role of the nanoconfinement strategy in maintaining electrode integrity.

Quantitative Analysis of Electrode Expansion

Quantitative measurements of the electrode cross-sections from SEM images (Fig. S10) before and after cycling show that the thickness of the pure SPAN electrode

increased from 23.89 μm to 40.86 μm, corresponding to a volume expansion rate of 71%. In contrast, the thickness of the SPAN/MMT electrode increased only from 24.79 μm to 34.61 μm, resulting in a much lower expansion rate of 39%. The rigid layered structure of MMT effectively suppresses the volume change of SPAN during cycling, which is a key factor enabling the ultra-long cycle life.

Supplementary Discussion on CV and EIS

CV Analysis: CV curves at different scan rates (Fig. S9a,c) were used to calculate the Li^+ diffusion coefficient (D_{Li^+}). According to the Randles-Ševčík equation, the peak current (I_p) shows a linear relationship with the square root of the scan rate ($\nu^{1/2}$) (Fig. S9 b, d). The slopes of the fitted lines for all redox peaks of the SPAN/MMT electrode are significantly greater than those of the SPAN electrode (Fig. S9e), indicating a higher Li^+ diffusion coefficient for SPAN/MMT. This directly proves that the ion channels provided by MMT accelerate ion transport.

EIS Analysis:

The EIS spectra (main text Fig. 3d) were fitted using the equivalent circuit. The fitted charge transfer resistance (R_{ct}) of SPAN/MMT (166.1 Ω) is substantially lower than that of pure SPAN (521.1 Ω). This indicates that the introduction of MMT significantly reduces the energy barrier for the electrode reaction and accelerates the reaction kinetics, which is fully consistent with the results from the CV and rate performance tests.

Ionic Conductivity Analysis:

To elucidate the role of MMT in the composite, EIS was performed on pure MMT

powder pellets (Figure S11). The results indicate an ionic conductivity of 1.55×10^{-3} S cm^{-1} for pristine MMT at room temperature, directly confirming the high ionic conductivity of its layered structure. This provides strong evidence that MMT serves as an effective ionic channel within the SPAN/MMT composite. Therefore, beyond acting as a nanoreactor that stabilizes the SPAN structure via confinement effects, the intrinsic ionic conductivity of MMT furnishes additional pathways for rapid Li^+ transport. This finding is consistent with the observed reduction in charge-transfer resistance (R_{ct}) and the improved reaction kinetics of the SPAN/MMT electrode.

Formula for calculating ionic conductivity:

$$\sigma = \frac{L}{R \cdot A}$$

where L is the pellet thickness, A is the electrode contact area, and R is the bulk resistance obtained from the low-frequency intercept of the Nyquist plot.

Table S1. The Raman characteristic peaks of SPAN/MMT under 532.8 nm laser excitation.

Wavenumbers (cm^{-1})	**Assignment**
309	C-S in plane bending
367	C-S
476	S-S
936	Ring (containing S-S bond) Stretch
1325	D band
1559	G band

Table S2. Slopes from the linear fitting of peak currents vs. square root of scan rate for SPAN and SPAN/MMT, and the calculated Li^+ diffusion coefficients (D_{Li^+})

Electrode	Redox Peak	Slope from I_p vs. $v^{1/2}$ (A $s^{1/2}$ $V^{-1/2}$)	Calculated D_{Li^+} (10^{-5} cm^2 s^{-1})
SPAN	C1 (~ 1.7 V)	4.50	5.67
	C2 (~ 2.0 V)	3.18	2.83
	A1 (~ 2.4 V)	7.52	15.8
SPAN/MMT	C1 (~ 1.7 V)	7.63	16.3
	C2 (~ 2.0 V)	5.76	9.29
	A1 (~ 2.4 V)	11.73	38.5

The lithium-ion diffusion coefficients (D_{Li^+}) for the SPAN and SPAN/MMT cathodes were calculated from the cyclic voltammetry (CV) curves at various scan rates (0.05, 0.1, 0.15, and 0.2 mV s^{-1}). The calculation was based on the Randles-Ševčík equation (equation 1) for reversible systems:

$$I_p = 2.69 \times 10^5 n^{1.5} A D_{Li^+}^{0.5} C_{Li}^{+} v^{0.5} \quad (1)$$

where I_p is the peak current (A), n is the number of electrons transferred per reaction molecule (taken as n=2 for lithium-sulfur batteries), A is the electrode area (cm^2), D_{Li^+} is the lithium-ion diffusion coefficient (cm^2 s^{-1}), $C_{Li+}$is the concentration of Li^+ in the electrolyte (mol cm^{-3}), and v is the scan rate (V s^{-1}).

Table S3. Comparison of the electrochemical performance of the cathode of SPAN/MMT with that of the previously reported SPAN

Material	Ratio of Active Material (wt%)	Current Density	Capacity (mA h g^{-1})	Ref.
BP-SPAN	43.0	1 C	845, 200th	[1]
$Se_{0.06}$SPAN	41.0	0.4 A g^{-1}	881, 800th	[2]
SPAN/RGO	44.0	0.1 C	1100,200th	[3]
SPAN-F3	52.8	0.2 C	777, 200th	[4]
I-SPAN	36.85	1 A g^{-1}	1201, 400th	[5]
PAN-S-VA	36.0	0.25 C	477, 200th	[6]
Co_{10}-SPAN-CNT	41.90	1 C	1020, 1500th	[7]
SFPAN	45.60	0.3 A g^{-1}	1200, 400th	[8]
$Se_{0.071}S_{0.929}$PAN NS	43.08	0.2 A g^{-1}	$322_{composite}$, 200th	[9]
SPAN-1.5%HBO	54.24	1 C	734, 100th	[10]
SPAN@CF-RGO	22.0	2.5 C	584.3, 300th	[11]
FeS_2/SPAN	53.54	1 C	588.16, 300th	[12]
SPAN@CDW	34.8	0.1 C	1350, 500th	[13]
SPAN/MMT	27.73	3 A g^{-1}	436, 5000th	This work

References

[1] S. Ma, Y. Wang, C. Fu, Y. Ma, Y. Gao, G. Yin, P. Zuo, *Chem Commun (Camb)* **2020**, *56*, 12797-12800.

[2] X. Chen, L. Peng, L. Wang, J. Yang, Z. Hao, J. Xiang, K. Yuan, Y. Huang, B. Shan, L. Yuan, J. Xie, *Nat Commun* **2019**, *10*, 1021.

[3] J. Li, K. Li, M. Li, D. Gosselink, Y. Zhang, P. Chen, *Journal of Power Sources* **2014**, *252*, 107-112.

[4] R. He, Y. Li, Z. Mu, H. Liu, Y. Zhang, X. Zhang, *ACS Applied Nano Materials* **2023**, *6*, 23163-23172.

[5] W. Xue, W. Xu, W. Wang, G. Gao, L. Wang, *Composites Communications* **2022**, *30*.

[6] H. Chen, C. Wang, C. Hu, J. Zhang, S. Gao, W. Lu, L. Chen, *Journal of Materials Chemistry A* **2015**, *3*, 1392-1395.

[7] A. Abdul Razzaq, G. Chen, X. Zhao, X. Yuan, J. Hu, Z. Li, Y. Chen, J. Xu, R. Shah, J. Zhong, Y. Peng, Z. Deng, *Journal of Energy Chemistry* **2021**, *61*, 170-178.

[8] J. Xiang, Z. Guo, Z. Yi, Y. Zhang, L. Yuan, Z. Cheng, Y. Shen, Y. Huang, *Journal of Energy Chemistry* **2020**, *49*, 161-165.

[9] K. Wang, T. Zhao, Y. Liu, T. Yu, G. Chen, W. Tang, L. Li, F. Wu, R. Chen, *Chemical Engineering Journal* **2024**, *487*.

[10] X. Zhang, H.-C. Lu, C.-R. Hao, J.-Q. Liu, X.-R. Kong, J.-L. Wang, *Chemical Engineering Journal* **2024**, *500*.

[11] J. Lu, Y. Zhang, J. Huang, H. Jiang, B. Liang, B. Wang, D. He, H. Chen, *Journal of Energy Storage* **2025**, *118*.

[12] C. Hao, J. Liu, Q. Wang, L. Wang, X. Zhang, J. Yang, Y. NuLi, H. Lu, J. Wang, *ACS Nano* **2025**, *19*, 25385-25394.

[13] S. M. Sabet, N. Sapkota, S. Chiluwal, T. Zheng, C. M. Clemons, A. M. Rao, S. Pilla, *ACS Sustainable Chemistry & Engineering* **2023**, *11*, 2314-2323.